

Supporting Information for Bubble-Free Electroosmosis With Propylene Carbonate

by

Deepa Sritharan, Abraham Simpson Chen, Prabhath Aluthgama, Bilal Naved,
and Elisabeth Smela*

Department of Mechanical Engineering and the Institute for Systems Research,
University of Maryland, College Park MD, USA

1 Device Fabrication

1.1 Devices for Flow Rate Measurement

Figure 1 illustrates the procedure used to fabricate the microfluidic devices for measuring EO flow rates. A photograph of the final device is shown in Figure 2. These were fabricated in polydimethylsiloxane (PDMS) by soft lithography using an SU-8 mold.

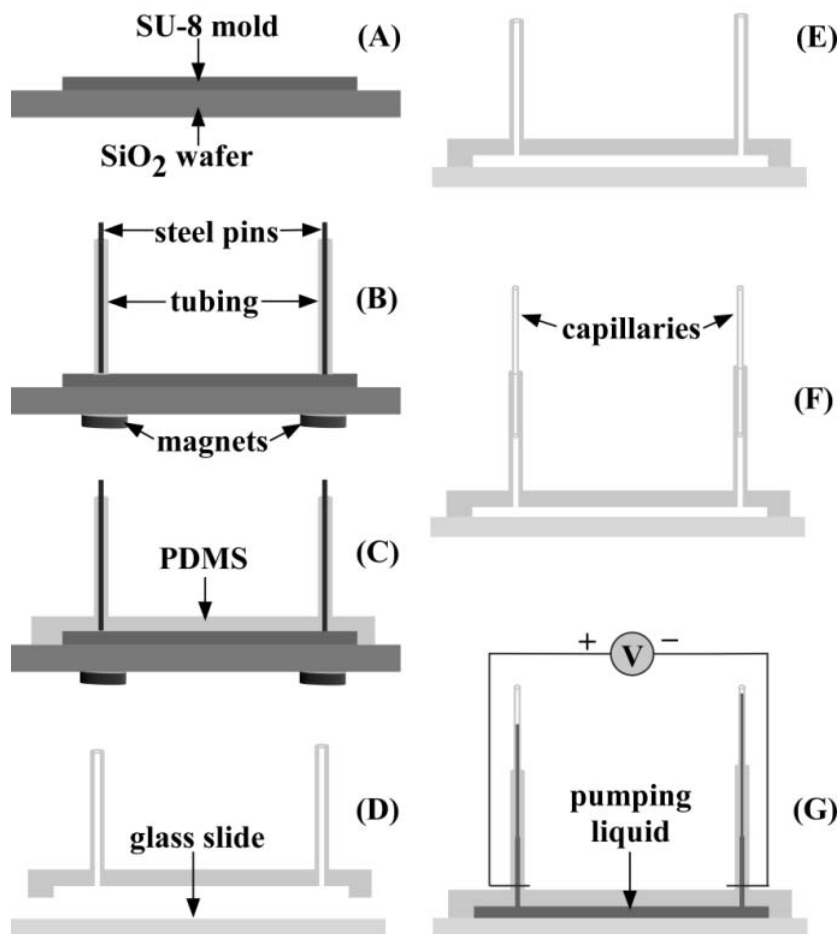


Figure 1. Fabrication of devices for measuring velocity of electroosmotic flow. (A) The SU-8 mold was fabricated by photolithography. (B) Two magnets were fixed under the wafer using PDMS, one positioned beneath each reservoir. To make the inlet and outlet, a piece of silicone tubing was placed on each reservoir. A steel pin were inserted into each tube and aligned with the magnets to hold the tubes upright. (C) The PDMS mixture was poured over the SU-8 mold around the tubes. The PDMS was cured at 60 °C on a hotplate oven for 45 minutes. (D) The resulting replica consisted of molded microchannels with attached inlet and outlet tubing. (E) The replica was oxygen plasma bonded to a glass borosilicate slide. (F) Glass capillaries were inserted into the inlet and outlet tubes. (G) Electrodes were pierced through the side of the tubing and connected to a high voltage power supply.

The SU-8 was spin-coated onto a silicon wafer at 500 rpm for 5 sec with 100 rpm/s acceleration and then at 2000 rpm for 1 min with 100 rpm/s acceleration. The edge bead was removed from around the wafer, and the device was allowed to rest for 30 minutes at room temperature. The wafer was pre-baked at 65 °C for 5 min and then at 95 °C for 15 min. The sample was cooled to room temperature over 10 min. The SU-8 was exposed to UV light (9 mJ/cm²) for 20 sec through the mask, then post-baked at 65 °C for 5 min and then at 95 °C for 15 min. The pattern was developed in SU-8 developer (Microchem, Newton, MA) to produce the mold. Thicknesses were measured by mechanical profilometry (Tencor AlphaStep 200). The final mold had an average height of 60 μm.

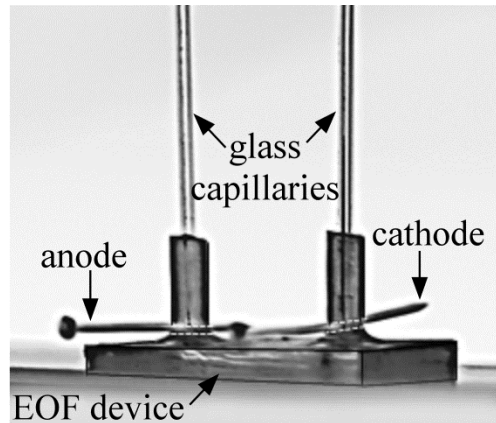


Figure 2. Photograph of a microfluidic device fabricated for measuring electroosmotic flow rate.

1.2 Devices for Measurement of Electroosmotic Actuation

In order to measure pressure generated by EOF, closed systems were prepared as shown in the photograph of the assembled device in Figure 3 and delineated in the schematic shown in Figure 4.

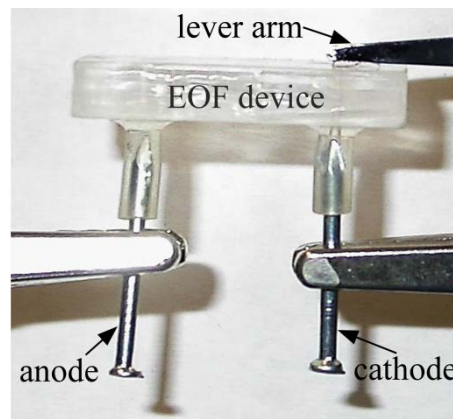


Figure 3. Photograph of a microfluidic device fabricated for measuring actuation of a PDMS membrane by electroosmotic flow.

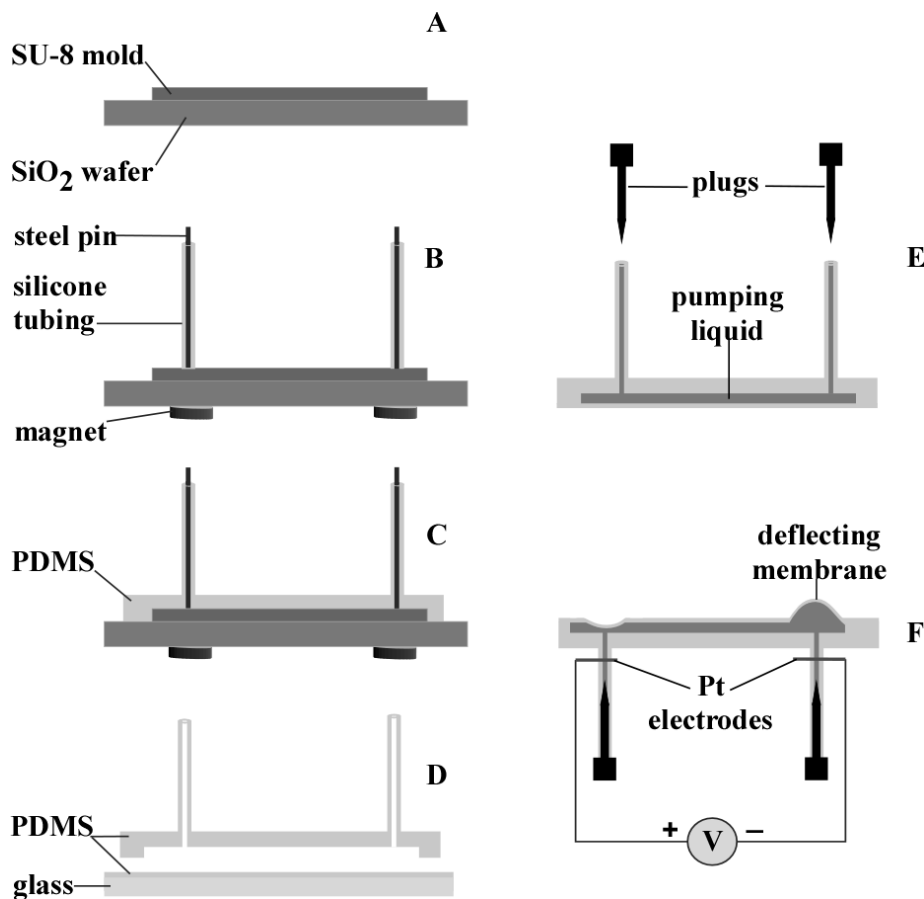


Figure 4. Fabrication of devices for measuring pressure. (A-C) Steps were the same as (A-C) in Figure 1. (D) A thin layer of PDMS was spin-coated onto a glass slide. The replica molded PDMS layer was plasma-bonded to the spincoated PDMS. (E) The device was filled with liquid and sealed by inserting steel pins to plug the tubing. (F) High voltage was applied across the steel electrodes.

2 Voltammetry

Steel electrodes were used for flow rate and actuation measurements. To assess the reactivity of the steel electrodes with the PC, we performed cyclic voltammetry (Figure 5) in DI water, PC, and PC with 1 mM TBTF.

The voltammograms on steel in DI and PC + TBTF differed from those on Pt, due to reactions with the water and the salt. It is interesting to note, however, that the current with anhydrous PC without salt was still small (the maximum current was 1.8 μA) and increased linearly with voltage. Currents on steel electrodes were approximately 3 times higher than currents on Pt in all three solutions.

For PC with salt on the platinum electrodes, Faradaic reactions started at 2.2 V, and multiple peaks were observed. On the steel electrodes, a sharp increase in current occurred at 1.3 V. The current increased steadily, with no peaks.

The shape of the DI water curve on steel was also different from that on platinum. On platinum currents became appreciable at 1.2 V, as expected from the literature. On steel, the curve looked Ohmic, as seen for PC without salt, but with a higher slope. There are no published voltammograms on steel available for comparison with our data.

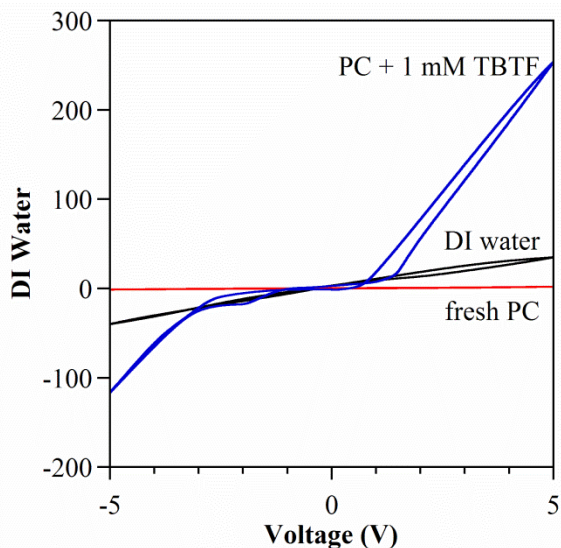


Figure 5. Cyclic voltammograms on steel electrodes in deionized water, PC, and PC with 1 mM TBTF salt (vs. Ag/AgCl, 200 mV/sec).

3 Color Version of Figure 2

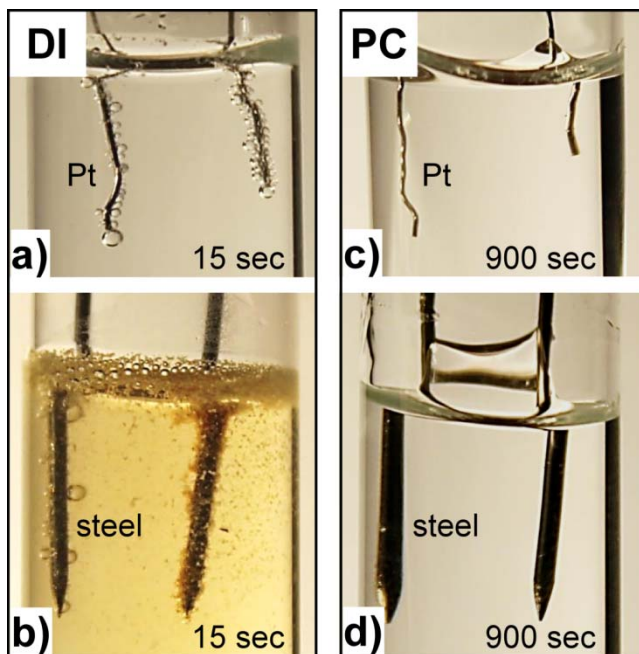


Figure 6. Color version of Figure 2 in the main text showing the water turning yellow with steel electrodes.

4 EOF Velocity

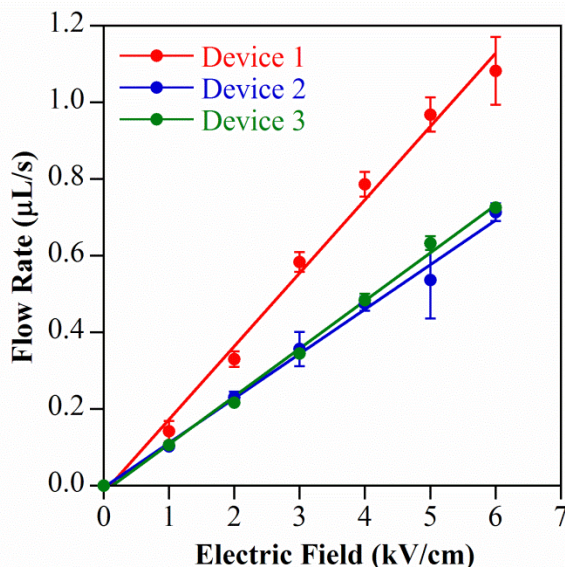


Figure 7. Repeatability of electroosmotic flow rates illustrated by measurements in three nominally identical devices.

In this section we present additional flow measurement data. The electroosmotic velocity of propylene carbonate was measured in three separate devices. Three velocity measurements were made at each voltage. The initial wetted length was 1 cm. After each cycle (turning the voltage on and off once) the voltage was left off for 10 seconds to allow the liquid to come to rest at the starting position to avoid back-pressure effects. The applied voltage was systematically increased for Device 1 (data shown in the paper) and Device 3, and the three repeats at each voltage being made one after the other. The voltages were randomized for Device 2. The data in Figure 7 were obtained by multiplying the measured velocity (mm/sec) by the cross-sectional area of the glass capillary (400 μm inner diameter).

Uncertainty Analysis

The uncertainty in velocity (v) can be determined by the propagation of errors in meniscus position (x) over time (t) [1]:

$$v = \frac{x}{t}$$

$$\Delta v = \sqrt{\left(\frac{\partial v}{\partial x} \Delta x\right)^2 + \left(\frac{\partial v}{\partial t} \Delta t\right)^2}$$

$$\Delta v = \sqrt{\left(\frac{1}{t} \Delta x\right)^2 + \left(\frac{-x}{t^2} \Delta t\right)^2}$$

The uncertainty in flow rate (f) is then $\Delta f = (\pi r^2)\Delta v$ where r is the inner radius of the glass capillary (200 μm). The uncertainty in the measurement was < 13% as shown in Table 1.

Table 1. Uncertainty analysis of flow rate for device 3, shown in Figure 4 of main paper.

Voltage (kV)	Meniscus Position 'X' (mm)	Mean of X	Standard Deviation of X	Ruler Uncertainty	Net Error ΔX	TIME 't' (sec)	Mean of t	Standard Deviation of t	Stopwatch Uncertainty	Net Error Δt	Net Error in Velocity Δv (mm/sec)	Net Error in Flow Rate ΔF ($\mu\text{L/s}$)	Mean Flow Rate F	% Relative Error $100*\Delta F/F$
1	10	10	0	0.5	0.5	11.9	11.8	0.30665	0.2	0.37	0.04968835	0.03122011	0.530973	5.87979
1	10					11.5								
1	10					12.1								
2	10	10	0	0.5	0.5	5.78	5.79	0.03215	0.2	0.2	0.10531589	0.06617193	1.084554	6.1013
2	10					5.83								
2	10					5.77								
3	10	10	0	0.5	0.5	3.69	3.65	0.04509	0.2	0.21	0.20632134	0.12963552	1.722994	7.52385
3	10					3.65								
3	10					3.6								
4	10	10	0	0.5	0.5	2.5	2.6	0.08888	0.2	0.22	0.37656574	0.23660323	2.41661	9.79071
4	10					2.63								
4	10					2.67								
5	10	10	0	0.5	0.5	1.93	1.99	0.05508	0.2	0.21	0.58274647	0.3661504	3.162677	11.5772
5	10					2.04								
5	10					1.99								
6	10	10	0	0.5	0.5	1.71	1.73	0.02082	0.2	0.2	0.7287943	0.45791496	3.624915	12.6324
6	10					1.75								
6	10					1.74								

5 Evidence for EO Flow

It can be difficult to determine the pumping mechanism for fluid flow under an electric field in a channel. Fast flow of PC also occurs in channels with diameters of 3 - 7 mm under fields of 1.5 to 3.5 kV/cm. Figure 8 shows a set-up that allows variation of the channel material and diameter. Tubes 2 cm long made of glass, polyethylene, or PDMS-coated glass were placed between the tips of two polyethylene pipettes. Needles (BD PrecisionGlide), serving as electrodes, were pierced through the pipettes (Samco Scientific 263-1S polyethylene transfer pipettes) just at the edges of the tubes, on either side. Openings were cut into the pipette bulbs to form open reservoirs for the PC.

With 30 gauge needles, the direction of flow was from the positive to the negative electrode. However, for larger sizes (23, 22, and 18 gauge) flow was in the opposite direction. The switch in direction was consistent when the experiments were replicated. The reversed flow using the 18 gauge needles was 50% faster than the forward flow using the 30 gauge needles at 3, 5, and 7 kV. This effect has previously been observed in electroconjugate flow experiments [2]. The flow rate depended on the tube material, suggesting that electroosmosis also contributed.

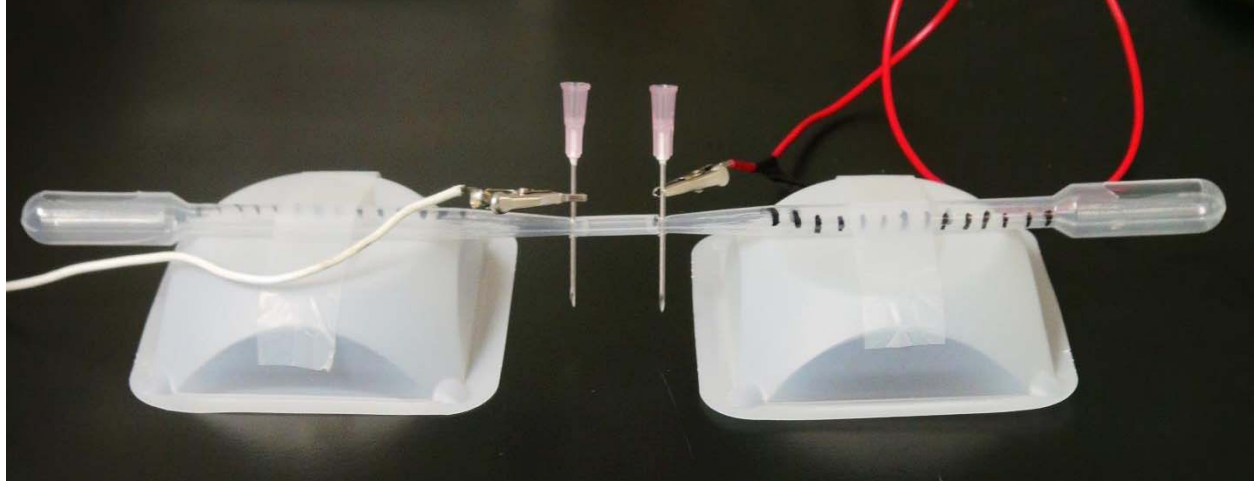


Figure 8. Experimental set-up for flow studies in meso-scale channels filled with PC. Syringe needles are used as electrodes on either side of a tube of varying material. The reservoirs in the pipette bulbs are open to the atmosphere.

When this experiment was conducted with the PDMS microchannels described in the main text, flow always occurred from the positive to the negative electrode, for both 18 and 30 gauge needles. (The device consisted of 9 microchannels connecting two open reservoirs, Figure 9, with the same 2 cm spacing between electrodes.) There was also no difference in flow rate between the two electrode sizes. These results are consistent with flow dominated by EO (wall effects) rather than electrode effects.

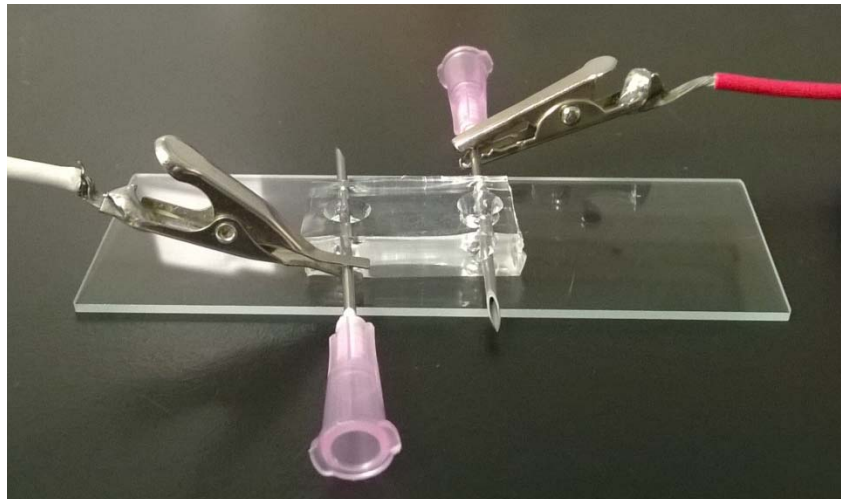


Figure 9. Experimental setup for flow studies in micro-channels.

6 Deflection at Increasing Voltage

The actuation behavior was similar in the three device that were tested. Deflections for a second device are shown in Figure 10.

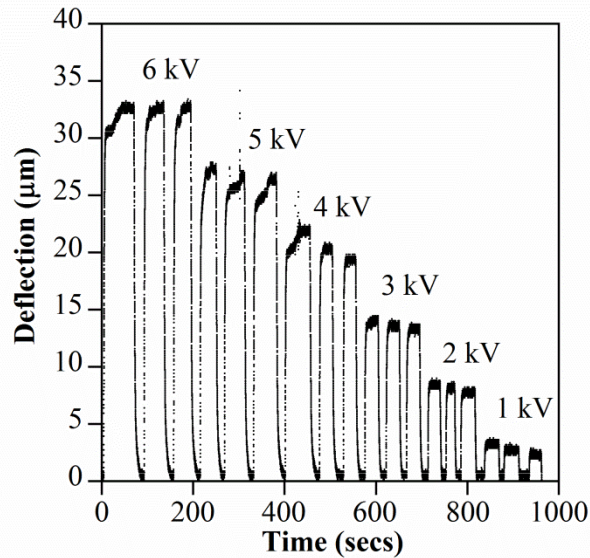


Figure 10. Membrane deflection in Device C versus time upon turning the voltage on and off 3 times each at voltages between 6 kV and 1 kV.

We took several precautions to prevent inconsistency.

- During fabrication, the same spin speeds were used to try to achieve the same membrane thickness (25 μm). The cast channel layers were made thick (3 mm) to prevent deformation during actuation, so that all the deformation occurred at the membrane. The filling tubes were placed exactly below the center of the membrane, determined visually. Devices were used at least one day after fabrication to allow surface charge induced during plasma bonding to dissipate.
- The device was filled with the same volume of liquid for each run, and trapped air bubbles were eliminated. If insufficient fluid was added, the membrane could stick to the bottom of the device.
- During fluid filling, the device was placed membrane-side down on a petri dish (to which it did not adhere) to prevent the required high filling pressures from bursting the membrane. The device was then flipped over for actuation.
- A constant electrode separation (1 cm) was maintained by visually ensuring the electrodes were inserted into the tubing to the same depth after filling the device.
- The force applied by the transducer to the membrane was calibrated before beginning each set of measurements.
- As described in the main text, in order to uniformly distribute the force applied by the transducer lever over the surface of the membrane, a small piece of transparency film was placed on the membrane.
- The transparency and lever arm were gently positioned over the membrane to minimize the possibility of the membrane sticking to the transparency. If the membrane adhered to the transparency, the shape of the bulged membrane changed, resulting in dissimilarities between readings and sudden jumps in lever position.
- Care was taken to position the lever tip precisely at the center of membrane.
- The lever was brought into contact with the transparency using a labjack by visually observing the reflection of the lever in the transparency.

- Before turning on the voltage we waited 10 seconds for the liquid to stop moving to avoid back-pressure effects.

Nevertheless, deflections and speeds varied between devices. Figure 11 shows a comparison of membrane deflection measurements in three devices, A (the device in Figure 6 of the main paper), B and C (the device in Figure 10), at voltages between 1 kV and 10 kV. Device B had more than twice the deflection of Device C.

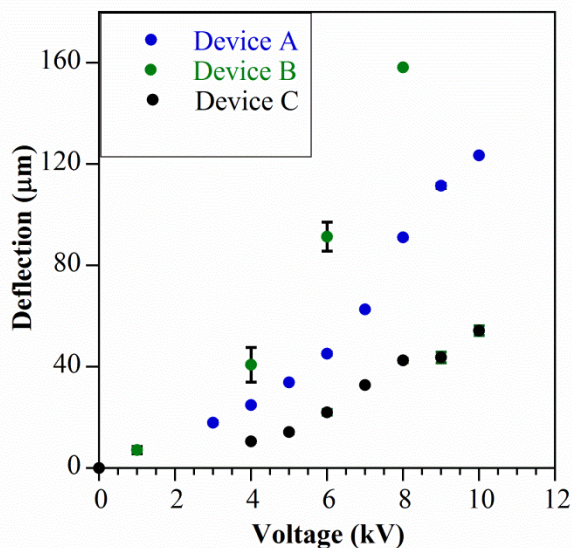


Figure 11. Repeatability of membrane actuation in different devices. Error bars indicate the standard deviation of five runs on the same device. In most cases, they cannot be seen because the variation is smaller than the size of the data point.

As shown in Figure 6 in the main paper, upon applying the voltage the membrane deflection initially increased rapidly and later plateaued. Similarly, when the voltage was turned off the membrane rapidly deflated and then slowly tapered off. At first glance, it appeared that the actuator displayed a first order response to the change in applied voltage. However, upon analysis it became apparent that multiple unknown processes with different time dependence were affecting the inflation/deflation. Future work will focus on understanding the causes of these variations. In addition, in future work the commercially available steel nail electrodes will be replaced with a more electrochemically inert and homogenous material, such as platinum or carbon, to eliminate the possibility of undesired electrochemistry.

Figure 12 is a close-up of the last inflation step in Figure 6 in the main paper, showing small oscillations at steady voltage. This effect may be due to the force-strain transducer. In isotonic mode, a constant lever force is applied and the displacement recorded. In our experiments this lever force deviated from the set value of 1 gram by ± 0.1 grams due to subtraction errors in the internal PID force control. One gram is close to the lower limit of the measurement capability of the transducer. Future research to increase the force generated by the actuator will allow greater lever forces to be applied, and thus more accurate readings. Future experiments will also be performed on a vibration-free platform to mitigate external disturbances.

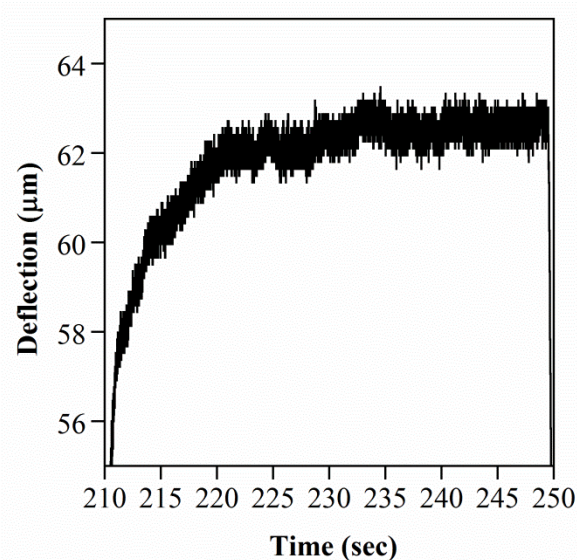


Figure 12. Close-up of the final membrane deflection in Figure 6 in the main paper. (7 kV).

7 Force Generation

The force generated by the actuator was determined experimentally by applying a constant force on the deflecting membrane via the force-strain transducer arm. The voltage was stepped on and off to 7 kV three times at each loading value, with loads increasing from 1 g to 15 g. The deflection decreased with load, as shown in Figure 13. The load curve was nonlinear, although deflection decreased almost linearly for loads greater than 5 g. The nonlinearity is most likely due to a decrease in contact area between the force distribution plate and the membrane at higher deflections.

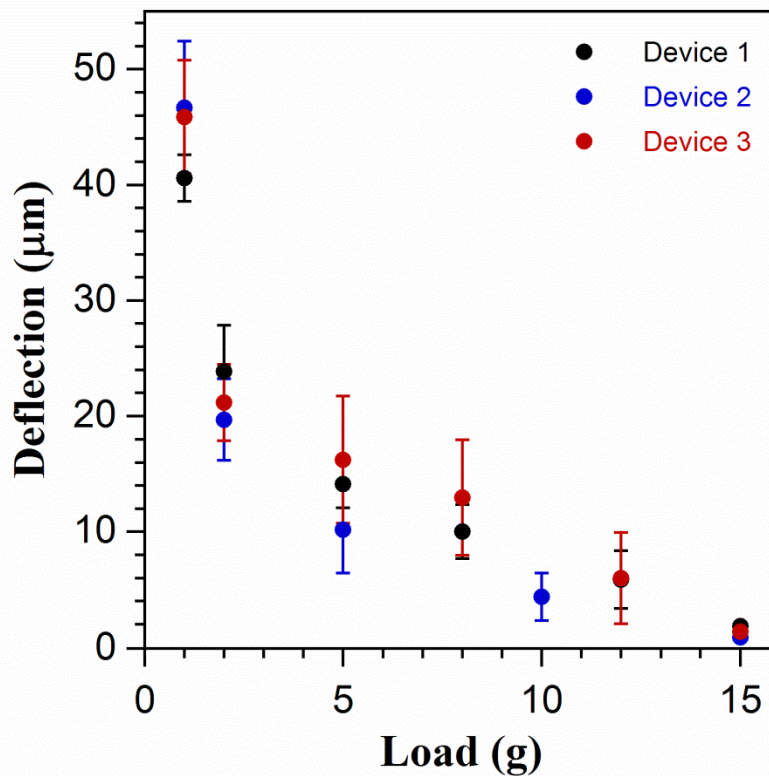


Figure 13. Load curve for three actuator devices. The load on the membrane was increased from 1 g to 15 g until no deflection was discernable.

The volumetric flow rate in the closed devices was determined by approximating the shape of the inflated membrane as a spherical cap with a base of diameter 5 mm and height equal to the deflection. (The base of the membrane was a 5x5 mm² square.) The average time for membrane inflation was 2.5 seconds. At 7 kV, for a deflection of 45 μm the calculated flow rate was 0.8 μL/sec. The flow rate in the closed actuator devices was comparable to the flow rate in the open configuration (SI Section 4). From Figure 7, the average flow rate for the three devices with the open configuration can be extrapolated to 0.85 μL/sec at 7 kV.

A pump curve is a graphical representation of a pump's ability to produce flow against a given pressure head. The pump curve was obtained by plotting the calculated flow rates for membrane filling against the applied pressure (load over the membrane surface area) (Figure 14).

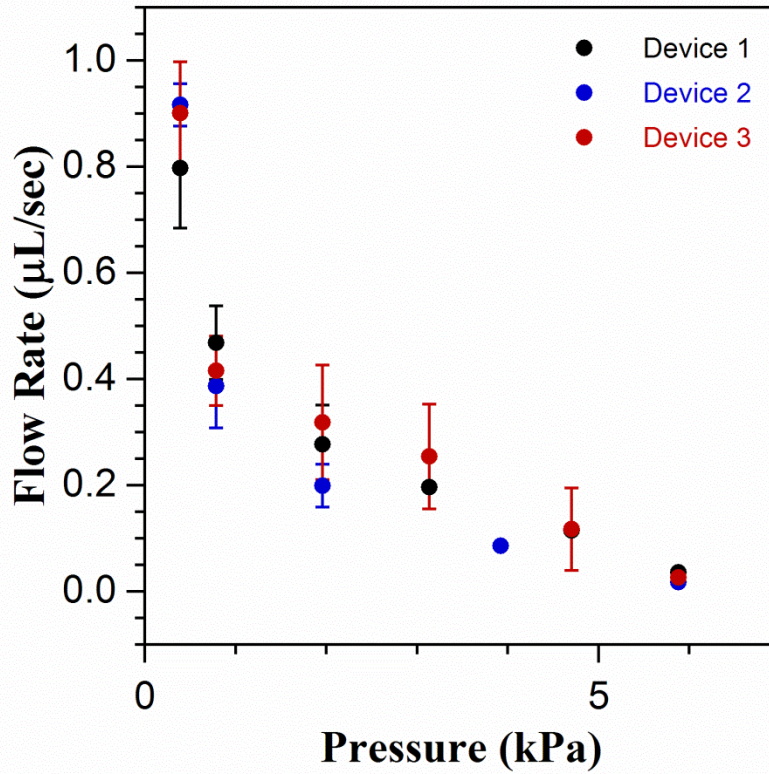


Figure 14. Pump curves for the three devices of Figure 13.

Deflection was blocked when a load of 15 grams was applied. This corresponds to a pressure of 6 kPa. At steady state, the EO flow rate is equal and opposite to the pressure-driven restorative flow rate, Q_p . Pressure-driven flow in the open device configuration is described by the Hagen-Poiseuille equation for flow in rectangular channels (Equation 1)[3].

$$\text{Equation 1: } Q_p = \Delta P \frac{n(d_c^3 w_c)}{12\mu L_c} \left[1 - 0.63 \frac{d_c}{w_c} \right]$$

Here ΔP is the pressure drop across the channels, n is the number of channels, d_c is the channel depth (41 μm), w_c is channel width (150 μm), L_c is channel length (1 cm), and μ is viscosity of PC (2.5 cp). For a pressure drop of 6 kPa the expected flow rate is 1.5 $\mu\text{L}/\text{sec}$, which is in reasonable agreement with the open system flow rate of 0.85 $\mu\text{L}/\text{sec}$ at 7 kV when the minimum load of 1 g was applied.

The flow rates in the open configuration were obtained by observing the meniscus in cylindrical glass capillaries attached to the microchannel devices. The flow rate in the capillary must be equal to the flow rate within the device, so it would be expected that the pressure drops would also be equal. Equation 2 describes pressure driven flow in a cylindrical channel.

$$\text{Equation 2: } Q_p = \Delta P \frac{\pi d_c^4}{128\mu L_c}$$

When the pressure drop required for a flow rate of 0.85 $\mu\text{L}/\text{sec}$ was estimated based on capillary dimensions (length 1 cm, inner diameter 400 μm), the value obtained was much smaller (34 Pa instead of 6000 Pa). This may be due to pressure losses due to surface tension forces, or because the effective inner diameter was smaller: the pressure drops match if 100 μm is used instead of 400 μm . The flow rate is highly sensitive to the radius (r^4).

We also modeled the membrane as a thin homogeneous membrane stretched by a uniform load over an opening in a rigid base [4] (Figure 15). At equilibrium, balancing the forces results in Equation 3, subject to the boundary condition $z=0$ along the edge of the membrane.

Equation 3:
$$\frac{\partial^2 z}{\partial x^2} + \frac{\partial^2 z}{\partial y^2} = -\frac{p}{T}$$

Here, p is the applied load and T is the tension in the membrane.

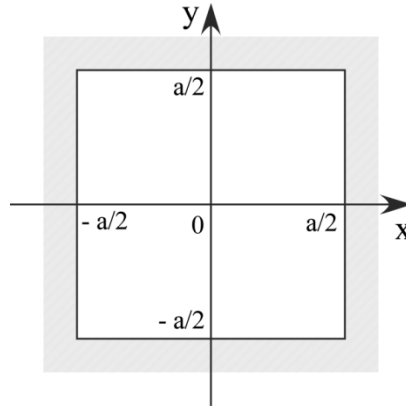


Figure 15. The undeflected membrane has a square surface of side $a = 5$ mm and is fixed along all edges to the surrounding PDMS base.

To non-dimensionalize the equation, we made the substitution $z = \frac{p}{2T} \phi$. Equation 3 then becomes:

Equation 4:
$$\frac{\partial^2 \phi}{\partial x^2} + \frac{\partial^2 \phi}{\partial y^2} = -2$$

subject to the boundary condition $\phi = 0$ along the edge of the membrane. The solution to this equation is

Equation 5:
$$\phi(x, y) = \frac{a^2}{4} + \frac{1}{2}(y^2 - x^2) - \frac{8a^2}{\pi^3} / \sum_{n=0}^{\infty} \frac{(-1)^n}{(2n+1)^3} \frac{\cosh k_n y}{\cosh(k_n a / 2)} \cosh k_n x$$

Maximum deflection occurs at the center of the membrane $(x, y) = (0,0)$. From Equation 5, for $a = 5$ mm,

Equation 6:
$$\phi(0,0) = 6.32 = \phi_{max} = \frac{2T}{p} z_{max}$$

Hooke's law for isotropic materials in two-dimensional compliance matrix form, in the absence of shear forces, is given by [5]

$$\text{Equation 7: } \begin{bmatrix} \varepsilon_x \\ \varepsilon_y \end{bmatrix} = \frac{1}{E} \begin{bmatrix} 1 & -\nu \\ -\nu & 1 \end{bmatrix} \begin{bmatrix} T_x/t \\ T_y/t \end{bmatrix}$$

The strain ε and tension T were assumed to be equal in the x and y directions; this was verified in the Abaqus simulation. Stress in the thin membrane is given by T/t .

$$\text{Equation 8: } \varepsilon = \frac{1}{E}(1-\nu)\frac{T}{t}$$

In our case the membrane thickness t was $25 \mu\text{m}$, and the Poisson's ratio ν for PDMS was assumed to be 0.5 [6]. Tension in the membrane at maximum deflection is then:

$$\text{Equation 9: } T_{\max} = \frac{Et\varepsilon_{z_{\max}}}{1-\nu}$$

Based on a deflection of $45 \mu\text{m}$, the strain $\varepsilon_{z_{\max}}$ was calculated as shown below.

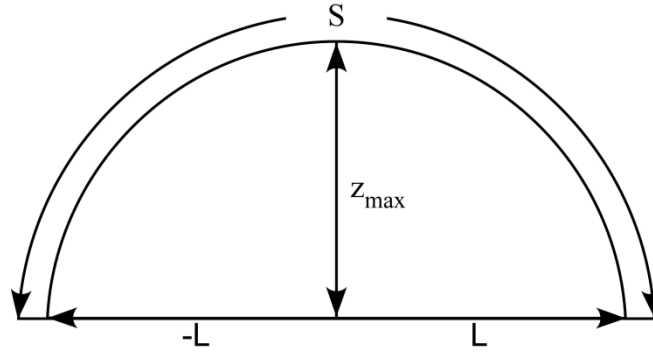


Figure 16. Cross-sectional view of the inflated membrane. The uninflated membrane has an initial length of $a = 2L = 5 \text{ mm}$. At maximum deflection z_{\max} the membrane assumes a parabolic profile of arc length S .

$$\text{Equation 10: } \varepsilon_{z_{\max}} = \frac{S - 2L}{2L}$$

where the arclength S is given by:

$$\text{Equation 11: } S = \int_{-L}^L \sqrt{1 + \left(\frac{dz}{dx}\right)^2} dx = 2 \int_0^L \sqrt{1 + \left(\frac{dz}{dx}\right)^2} dx$$

Substituting,

$$\text{Equation 12: } \varepsilon_{z_{\max}} = \frac{2 \int_0^L \sqrt{1 + \left(\frac{dz}{dx}\right)^2} dx - L}{L}$$

For a parabolic segment,

$$\text{Equation 13: } z = z_{\max} \left(1 - \frac{x^2}{L^2} \right)$$

Differentiating Equation 13:

$$\text{Equation 14: } \frac{dz}{dx} = \frac{-2z_{\max}x}{L^2}$$

Substituting Equation 14 into **Error! Reference source not found.** and integrating between $L = 0$ mm and $L = 2.5$ mm, a deflection value of $z_{\max} = 45$ μm gives a strain $\epsilon_{z_{\max}} = 0.054\%$. Using Equation 6 and Equation 9, the calculated modulus is 1.8 GPa. The modulus of PDMS has been reported to be 4 MPa [7]. Thus the deflection was greatly overestimated by this model: using a modulus of 4 MPa predicted a deflection of 1.5 mm, 30 times larger than the experimentally observed value. This leads us to conclude that the deflection cannot be described exclusively by a membrane stretching model and that additional factors must be considered in the force balance.

8 Characterization of PC Degradation in the Presence of Moisture

Electrochemical decomposition of an electrolyte can result in the formation of gases, deposits at the solid-electrolyte interface, and/or the dissolution of species in the electrolyte. Understanding the degradation reactions in PC with moisture may be helpful to devising methods to alleviate them. Numerous groups, specializing in battery applications of PC, have attempted to characterize its electrochemical decomposition [8], and this remains an open topic of research.

Most studies have been conducted in anhydrous PC containing salts of lithium, sodium, or potassium, in which the reaction products are strongly influenced by the cation. The alkali metal ions have been reported to trigger reactions, such as polymerization and cleavage, that lead to the observed to exacerbate the problem of degradation [8]. This may be because the H^+ produced by the splitting of water electrophilically attacks the PC [8], resulting in ring opening.

In previously published work, we have shown that even without salt, degradation of PC occurs upon exposure to moisture [9], leading to higher currents and reduced mobility. (PC is not affected by either visible or UV light.) More recently we have observed that exposure to a very small amount of room air, such as storage in non-airtight vials, can irreversibly affect the PC. We therefore investigated the degradation products using Fourier transform infrared spectroscopy (FTIR), surface-enhanced Raman spectroscopy (SERS), and X-ray photoelectron spectroscopy (XPS) (which is performed under high vacuum).

8.1 Fluid Degradation

Degraded PC was produced by exposing it, in a beaker, to high ambient humidity (85-90%) for one week. Electrolysis of half of this PC then was conducted with steel electrodes (62-0167 GEM, Personna American Safety Razor Company, New Jersey). A constant voltage of 1000 V was applied to the electrodes (separated by 2 cm) for 5 hours, during which time the current

increased from 1 to 6 mA (the resistance between the electrodes decreased) and a yellow deposit formed on the anode. The deposit was non-uniform in color and thickness. The electrolyzed PC acquired a yellow tinge, and some bubbles formed at the anode.

In another vial, PC was exposed to similar humid conditions, and in a similar set up, electrolysis at 1000 V was conducted using platinum electrodes (fabricated by electron beam deposition of 800 nm Pt over a 200 nm Ti adhesion layer on an oxidized silicon wafer) for 5 hours. Currents were 1-2 mA and remained constant. A faint white deposit formed on the anode, with no change in electrolyte color. The deposit on the steel appeared to be much thicker than the deposit on the platinum.

8.2 Methods

8.2.1 FTIR

A Thermo Nicolet NEXUS 670 FTIR was used with an attenuated total reflectance (ATR) accessory. Liquids were analyzed by directly dispensing a drop on the ATR window. The electrodes with deposits were placed directly onto the ATR window; bare steel and platinum were used as controls. Deposits were scraped off the electrodes and encased in a potassium bromide (KBr) pellet (KBr is transparent to IR light) by milling the deposit with KBr to form a fine powder and compressing it.

Omnic spectroscopy software was used to collect and analyze data. The spectral range was 400 - 4000 cm^{-1} ; 20 scans were averaged per spectrum. The analysis chamber was purged with nitrogen for 15 minutes to minimize large absorbance peaks from water and carbon dioxide in air.

Samples were also sent to Shimadzu Scientific Instruments Inc. (Columbia, Maryland), for expert analysis using FTIR reflectance microscopy. The Shimadzu IR Prestige-21 spectrophotometer was used in conjunction with the Shimadzu AIM-8800 microscope in the reflectance mode. LabSolutions IR 2.02 software was used for data collection and analysis. AimView32 Ver. 2.0 control software was used with the Shimadzu AIM-8800. The spectral range was 700 - 4000 cm^{-1} , and 50 scans were averaged per spectrum.

8.2.2 SERS

Surface enhanced Raman spectroscopy (SERS) was performed with a Horiba Yvon LabRam ARAMIS Raman microscope. A 532 nm laser source rated at 100 mW, with an optical density filter (D1) with 10 % transparency, was used for excitation. A 5 sec exposure time was used, and spectra were averaged over 10 scans. The device was calibrated using a silicon standard to a characteristic Raman shift at 520.7 cm^{-1} .

Electrolyte samples were placed on a glass slide using a syringe to dispense a 0.1 mL droplet. A 10 \times objective was used for focusing the excitation light on the droplet. The laser was focused on the electrode sample with a 100 \times objective.

8.2.3 XPS

XPS data for the steel and platinum electrodes were collected using a Kratos Axis 165 x-ray photoelectron spectrometer using monochromatic Al K α (1486.7 eV) radiation of 14 kV and 20 mA. Charge neutralization was required to minimize sample charging. Survey spectra were collected with a pass energy of 160 eV, while high resolution spectra were collected with a pass energy of 40 eV. The vacuum was maintained below 5×10^{-8} Torr throughout data collection. Peaks were referenced to adventitious carbon (atmospheric hydrocarbons) at 284.8 eV. The survey scans were performed with a 300 ms exposure time. A single survey scan was performed on each sample. The exposure times for the high resolution scans were 350 ms, 260 ms, and 330 ms for platinum, carbon, and oxygen respectively. Ten scans were performed on each sample for high resolution data. Fitting was performed using CASA XPS software. Data were fit to peaks with a 70% Gaussian, 30% Lorentzian line shape.

XPS can probe to a depth of up to 10 nm. The composition of the deposit within that 10 nm was estimated in terms of atomic percentage, calculated by integration of the area under the peak in the survey scans [10].

8.3 Results

8.3.1 FTIR Analysis of PC

Freshly aliquoted PC (“fresh PC”), from a new, previously unopened bottle was used as a control. This was compared with PC exposed to humid air (“moisture-exposed PC”) and the PC exposed to humid air followed by electrolysis using steel electrodes (“electrolyzed PC”).

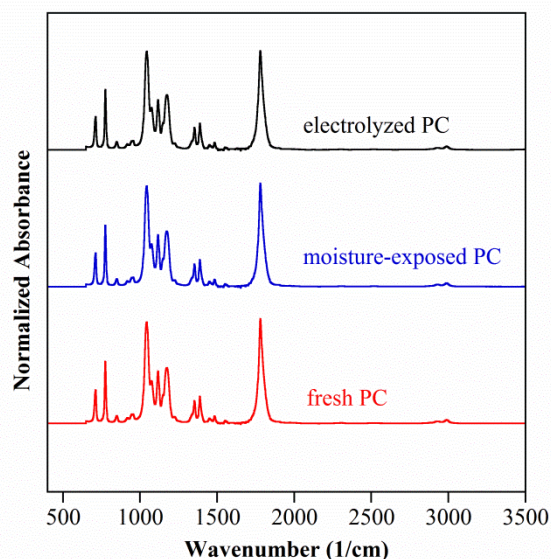


Figure 17. FTIR spectra of fresh PC (from a just-opened bottle), moisture-exposed PC (stored in a high humidity (85-90%) environment for 1 week), and electrolyzed PC (subjected to 5 hours of current flow at 1 kV after exposure to 85-90% humidity over a period of one week).

The FTIR spectra from the three liquids are shown in Figure 17. The spectrum for the fresh PC matched that in the literature [11, 12]. However, we were surprised to find that even after the PC was exposed to moisture and high electric fields (kV) the spectra remained unchanged. Upon electrolysis using the steel electrodes the initially colorless PC turned yellow (presumably due to formation of iron oxide, and gas bubbles and a deposit were produced. We had anticipated peaks suggesting oxidative decomposition products, such as acetone [13]. PC electrolyzed using platinum electrodes had the same spectrum. Our conclusion is therefore that the reaction products are present in too low a quantity to contribute to the spectra.

8.3.2 FTIR Analysis of Electrodes

Using the NEXUS 670, there were no peaks in any of the IR spectra (normalized to the pristine surfaces) from the anodes, despite the presence of the visible deposits. There were also no peaks from the deposits placed in the KBr pellets.

From the Shimadzu IRPrestige-21, peaks were obtained only from the steel anode. Spectra were recorded at multiple positions on the anode; the one shown in Figure 18 was obtained where the deposit was thick. The peak heights and positions varied appreciably at the different positions, suggesting that the deposit was inhomogeneous in thickness and composition. The main peaks are listed in Table 2 together with the corresponding bonds, based on IR reference tables [14-16]. These peaks suggest the formation of alcohol, ether, and amorphous carbon species.

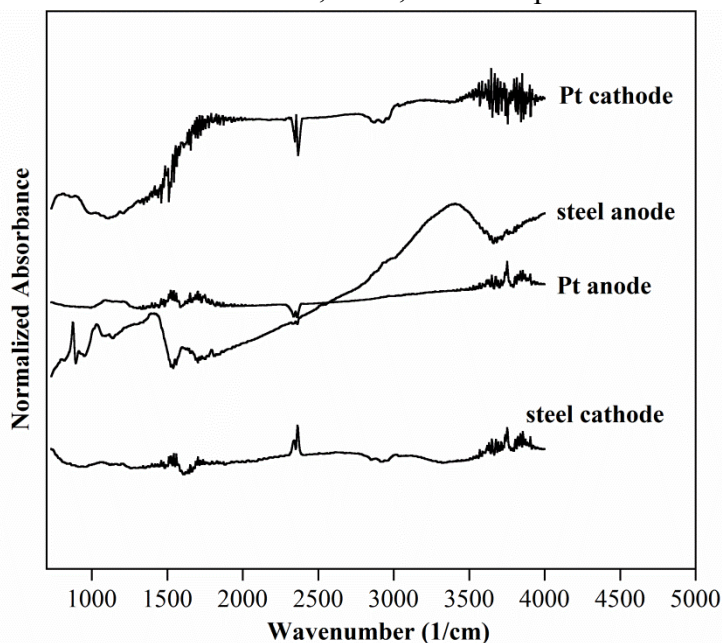


Figure 18. IR spectra of the surfaces of the steel and platinum electrodes after electrolysis of PC. The spectrum was obtained by FTIR reflectance microscopy from Shimadzu Inc.

Table 2. IR peaks from the deposit on the steel anode and the corresponding molecular bonds and possible functional groups.

Wavenumber, cm^{-1}	Molecular Bond [14-16]
3375	O–H stretch, H-bonded
2932	C–H stretch
1790	C=O stretch
1597	C–C stretch (in-ring)
1034	C–O stretch
872	C–H bend
389	C–H bend

8.3.3 Raman Analysis of PC

Raman spectra were obtained for fresh PC, moisture-exposed PC, and electrolyzed PC (Figure 19). There was no change after moisture exposure or degradation by electrolysis. This implies that the species formed by electrolysis were not detectable by SERS, either due to their low concentrations or because they contained bonds that were not Raman active.

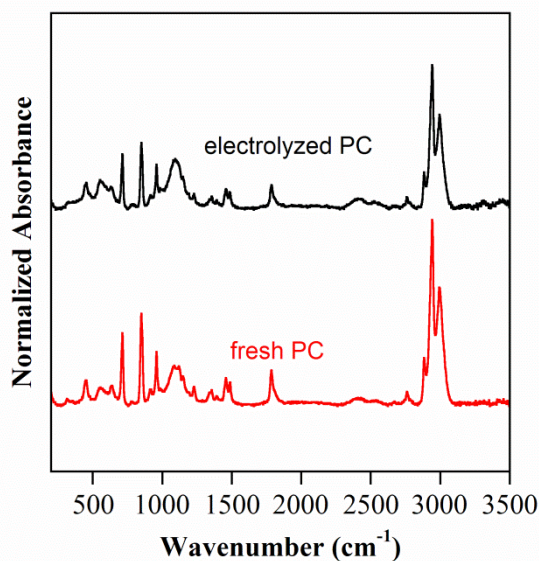


Figure 19. Comparison of Raman spectra of fresh PC and electrolyzed PC. The spectra had identical peaks.

8.3.4 Raman Analysis of Electrodes

No peaks were observed on the cathodes of either steel or platinum, but there were peaks on the anodes (Figure 20). The Raman spectra suggest that amorphous carbon and ether moieties constituted a significant portion of the deposit. The main peaks are listed in Table 3, together with the corresponding bonds.

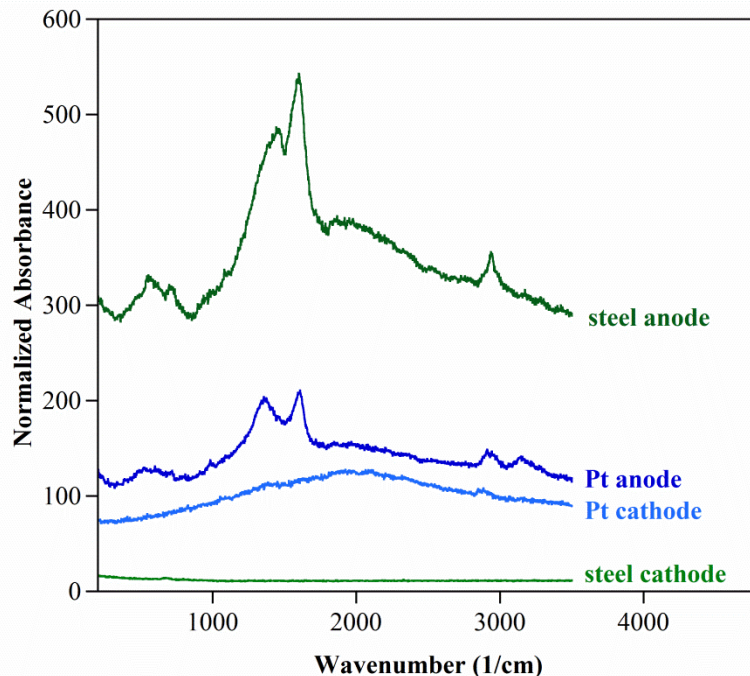


Figure 20. Raman spectra of deposits on steel and Pt anodes.

Table 3. Raman peaks and assignments for deposits on steel and platinum anodes.

Wavenumber, cm^{-1}	Molecular Bond [14-16]
≥ 3100 (steel, Pt)	O–H stretch
2932 (steel)	C–H stretch
2909 (Pt)	
1864 (steel)	C=O stretch
1843 (Pt)	
1606 (Pt)	C–C
1355 (steel)	C–C
935 (steel)	C–O–C stretch
809, 909, 982 (Pt)	
695 (steel)	
716 (Pt)	C–H bend
550 (steel)	C–C
597 (Pt)	

8.3.5 XPS Analysis of Steel Electrodes

Apart from iron, carbon, and oxygen, the steel control contained chromium, zinc, nickel, sodium (the most abundant, and persistent impurity), lithium, calcium, fluorine, nitrogen, and silicon. Some of these elements are likely to be involved in the reactions that occur at the electrodes [8]. The peak sizes of iron, carbon, oxygen, and sodium upon electrolysis are given in Table 4.

Table 4. Surface composition of steel electrodes from XPS survey scans.

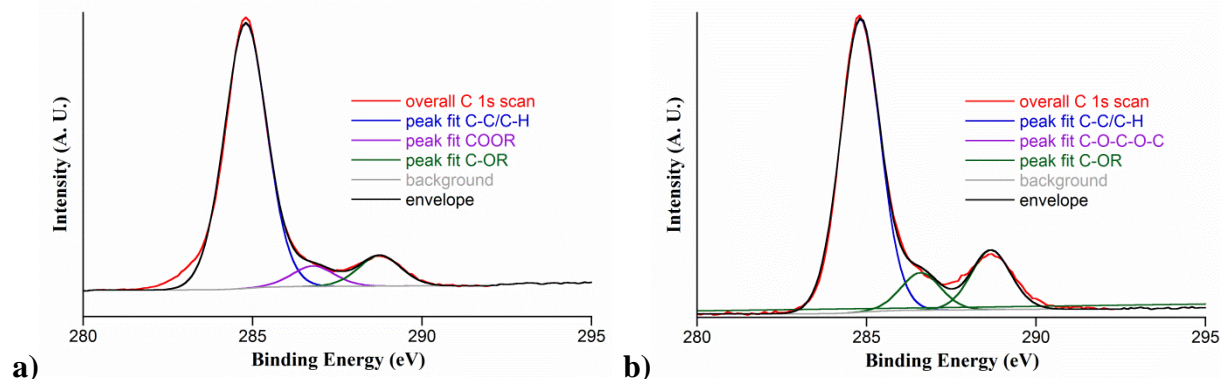
<i>Element Detected</i>	<i>Steel Control (atom%)</i>	<i>Steel Anode (atom%)</i>	<i>Steel Cathode (atom%)</i>
Na (1s)	0.61%	0%	0%
Fe (2p)	12.96%	3.38%	9.51%
C (1s)	44.78%	63.36%	50.97%
O (1s)	40.12%	32.62%	37.09%

The percentage of metallic iron decreased on the surfaces of both the anode and the cathode, accompanied by an increase in the percentage of carbon, consistent with the formation of a carbonaceous deposit. While sodium was present in the control sample, there was no sodium on either cathode or anode, suggesting that it had been dissolved into the electrolyte. (In order to test this hypothesis, the liquid was inspected by FTIR and Raman, but no sodium was seen; at these low concentrations, that is not surprising.)

When the electrolyte used with steel was subjected to electrolysis a second time, now using clean platinum electrodes, sodium (Na (1s) 0%) reappeared on the cathode (Na (1s) 7.11%), as verified by XPS spectroscopy. In the literature [17] this has been seen previously and attributed to electroplating from the solution. The presence of sodium as an impurity in steel could reduce the EO pumping efficiency by increasing the ionic strength of the PC and thereby lowering the zeta potential [18]. Sodium can also trigger carbonaceous deposit formation and degrade PC [8].

While it was expected that metal oxidation occurred at the anode, it was not possible to quantify the increase in iron oxides based on the high resolution scans for iron, or by comparison of the atomic percentage compositions from survey scans of the control and the anode. This is likely due to the presence of a large amount of native iron oxide species on the control.

However, the high resolution scan for carbon did confirm, by peak fitting, that on the anode carbonaceous products having carboxylic acid, alcohol, and ether groups were deposited (Figure 21a). At the cathode, carbonaceous deposits were formed having alcohol, ether, and polyether groups (Figure 21b).

**Figure 21. High resolution scan of steel a) anode and b) cathode for carbon species.**

8.3.6 XPS Analysis of Platinum Electrodes

The surfaces of the platinum electrodes after electrolysis were compared to the surface of a control sample of platinum (800 nm Pt on a 200 nm Ti adhesion layer on an oxidized silicon wafer). The results are summarized in Table 5.

Table 5. Surface composition (atom%) of platinum control from XPS survey scan.

Element	Platinum Control	Platinum Anode	Platinum Cathode	Platinum Passive
Na (1s)	0%	0%	13.18%	0%
Pt (4f)	48.19%	24.85%	8.46%	40.14%
C (1s)	43.90%	34.78%	30.39%	44.44%
O (1s)	7.91%	37.12%	45.44%	15.42%

The percentage of metallic platinum decreased on both anode and cathode, accompanied by an increase in the percentage of carbon and oxygen, indicating the formation of carbonaceous deposits. While no sodium was present on the control sample or anode, it appeared on the cathode, suggesting that it deposited as a contaminant from the electrolyte as suggested by [17]. The clips used to make electrical contact were a possible source of contamination. The sodium was difficult to eliminate despite careful experimental set up. Prior to electrolysis, all components that came in contact with the PC were cleaned of organics: the steel and platinum electrodes, the handling tweezers, and the steel clips used to make electrical contact were rinsed sequentially with acetone, methanol, isopropanol, and DI water. It has been reported that moisture, sodium, and other electropositive elements can trigger the formation of deposits through reductive electrochemical decomposition of PC [8]. Based on these data, to avoid deposit formation the solution must be maintained free of contaminants.

High resolution scans for platinum (Figure 22a) revealed Pt oxide on the anode, showing that the platinum anode had oxidized. The platinum electrodes therefore cannot be assumed to be completely inert, since they are affected when used with degraded PC. There was no change in the oxidation state of the platinum used as a cathode (Figure 22b).

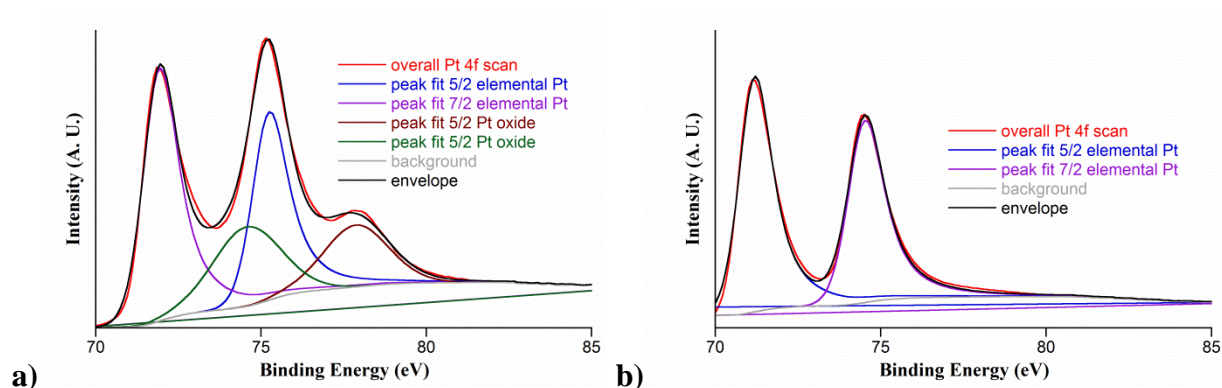


Figure 22. High resolution scan of platinum a) anode and b) cathode for platinum species.

The high resolution scan of the platinum anode for carbon confirmed that carbonaceous products with carboxylic acid, alcohol, and ether groups were deposited (Figure 23a). At the cathode,

carbonaceous deposits with alcohol, ether, and polyether groups were seen (Figure 23b). These results indicate that the products formed on steel and platinum were similar.

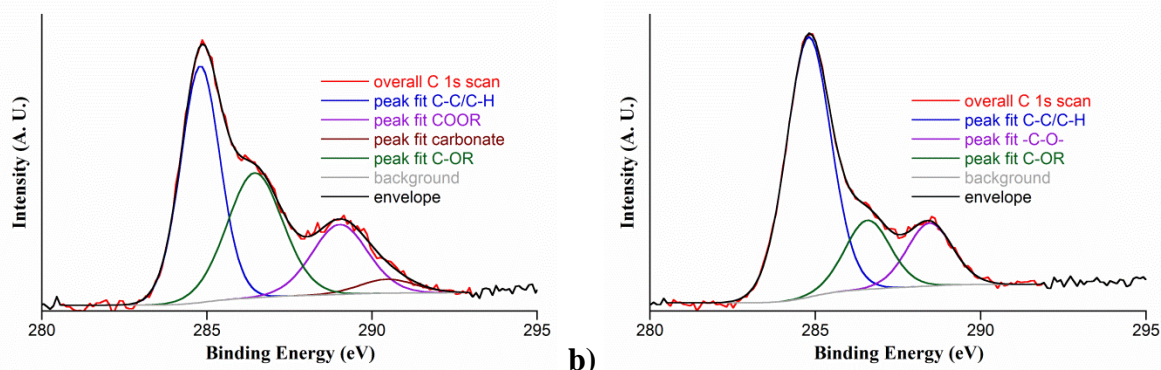


Figure 23. High resolution scan of the platinum a) anode and b) cathode for carbon species.

In order to verify that deposit was formed only on the electrodes used to apply the electric field, a platinum sample was placed in the electrolyte (electrically disconnected) to observe whether a deposit/precipitate formed (Platinum Passive in Table 5). The composition of the surface of this sample was similar to that of the control, confirming that deposits formed only when the platinum was connected to the voltage source.

8.4 Summary of Spectroscopy Results

PC was subjected to a humid environment and then to electrolysis. When electrolysis was performed with steel, the PC turned yellow. When electrolysis was performed with platinum, the PC remained colorless. FTIR and Raman did not have the sensitivity required to reveal the new species.

When electrolysis was performed with steel, a thick (~50 μm based on visual inspection) yellow deposit was formed on the anode. A much thinner white deposit was formed on the platinum anode. For both metals, spectroscopy revealed that the deposits contained alcohol, ether, and carboxylic acid groups. While neither steel nor Pt cathodes had a visible deposits, spectroscopy showed that alcohol, ether, and polyether groups were present. These findings are consistent with a prior study [8].

9 References

- [1] Ku, H. H., *J. Res. Nat. Bur. Stand.* 1966, 70, 263-273.
- [2] Mori, K., Yamamoto, H., Takemura, K., Yokota, S., Edamura, K., *Sens. Act. A* 2011 167 84-90.
- [3] Bruus, H., Oxford University Press, New York 2008, p. 51.
- [4] Sokolnikoff, I. S., *Mathematical theory of elasticity*, McGraw-Hill 1956.
- [5] Holzapfel, G. A., *Nonlinear Solid Mechanics: A Continuum Approach for Engineering*, Wiley 2000.
- [6] Pritchard, R. H., Lava, P., Debruyne, D., Terentjev, E. M., *Soft Matter*, 9, 6037-6045.
- [7] Liu, M., Sun, J., Sun, Y., Bock, C., Chen, Q., *J. Micromech. Microeng.* 2009, 19, 035028.
- [8] Xu, K., *Chem. Rev.* 2004, 104, 4303-4417.
- [9] Sritharan, D., Motsebo, M., Tumbic, J., Smela, E., *SPIE EAPAD*, SPIE Proceedings, San Diego, California, USA 2013.
- [10] Casa Software Ltd., 2008, pp. 1-7.
- [11] Smith, A. L., in: Carver, C. D. (Ed.), The Coblenz Society, pp. 1-24.
- [12] National Institute of Advanced Industrial Science and Technology.
- [13] Ufheil, J., Wursig, A., Schneider, O. D., Novak, P., *Electrochem. Commun.* 2005, 7, 1380-1384.
- [14] Pavia, D. L., Lampman, G. M., Kriz, G. S., Vyvyan, J. A., *Introduction to Spectroscopy: A Guide for Students of Organic Chemistry* W. B. Saunders Co., Philadelphia 1979, pp. 30-86.
- [15] Horiba Jobin Yvon, 2013, pp. 1-2.
- [16] Lambert, J. B., Shurvell, H. F., Cooks, R. G., Macmillan 1987, pp. 174-177.
- [17] Jorni, J., Tobias, C. W., *J. Appl. Electrochem.* 1975, 5, 279-290.
- [18] Kirby, B. J., in: Kirby, B. J. (Ed.), *Micro- and Nanoscale Fluid Mechanics: Transport in Microfluidic Devices*, Cambridge University Press 2010, pp. 199-218.